PAMAM-stabilized Pt–Ru nanoparticles for methanol electro-oxidation

Yunlong Gu [a], Gang Wu [a], Xiao Feng Hu [b], Donna A. Chen [b], Tara Hansen [b], Hans-Conrad zur Loye [b], Harry J. Ploehn [a],*

[a] Department of Chemical Engineering, University of South Carolina, Columbia, SC 29208, USA
[b] Department of Chemistry & Biochemistry, University of South Carolina, Columbia, SC 29208, USA

ABSTRACT

This work utilizes poly(amidoamine) dendrimers (PAMAM) as a protective ligand in solution to produce carbon-supported, Pt–Ru bimetallic nanoparticles for use as methanol electro-oxidation catalysts. UV–vis spectra show that after initial Pt^{2+} complexation with PAMAM G4OH dendrimer in water, appropriate adjustment of solution pH permits subsequent Ru^{3+} complexation without displacing Pt^{2+}, demonstrating the formation of an aqueous, bimetallic solution complex. Catalysts (nominally 20 wt% metals, confirmed by AA spectroscopy) are produced by impregnating high surface area carbon black with $G4OH–(Pt^{2+})_x(Ru^{3+})_y$ complex solution, drying, and activation in H_2 gas at elevated temperature. XPS results show that activation in H_2 at 400 °C removes virtually all of the PAMAM and reduces all of the Pt and most of the Ru to zero valence. TEM and XRD results show that the use of G4OH in the recipe is crucial for controlling metal particle size, and that the particles are crystalline with lattice parameters indicative of bimetallic Pt–Ru alloys. XRD data also suggest that G4OH promotes greater Pt–Ru alloying when Pt:Ru = 1:1. Catalytic activity for methanol oxidation increases with Ru content and is greatest for the catalyst with 1:1 Pt:Ru ratio. Per unit mass of Pt, the methanol oxidation activity of 20 wt% G4OH–PtRu/C catalyst is about 60% greater than that of E-Tek's commercially available 20 wt% PtRu catalyst.

© 2009 Elsevier B.V. All rights reserved.

1. Introduction

Direct methanol fuel cells (DMFCs) have emerged as a promising power source for automotive and portable power applications. The attractive aspects of DMFCs include ease in fuel handling, relatively simple system design, high efficiency, and low emissions [1,2]. However, practical implementation of DMFCs has been hindered by the slow reaction kinetics for methanol electro-oxidation on platinum. Methanol oxidation on Pt surfaces involves several steps including methanol adsorption and dissociation, water adsorption and activation, and CO oxidation [3]. The slow reaction kinetics may be due to strong adsorption of CO and $HCOO^-$ intermediates on Pt, leading to a low rate of site turnover.

In the search for more active catalysts, several Pt alloys have been investigated extensively [4,5]. Compared to pure Pt, Pt–Ru alloys have higher activity for methanol electro-oxidation as well as reasonable stability. Ruthenium may lower the water dissociation potential, providing more OH_{ads} to accelerate CO oxidation (the bi-functional effect [3]); it may also weaken CO adsorp-

tion by altering the electronic structure of Pt (the ligand effect [6,7]).

Understanding the mechanism of Pt–Ru catalysts for methanol electro-oxidation relies on characterization of their atom-scale structure. Recent XAS [8–10] and NMR [7,11,12] experiments have yielded much insight about the architecture and degree of alloying in Pt–Ru nanoparticles. XAS results [8–10] show that Pt–Ru nanoparticles prepared by different methods have a Pt-rich core surrounded by a Ru-rich shell containing considerable alloyed Pt. NMR results [11] suggest that high catalytic activity requires surface enrichment of metallic Ru. In general, superior catalytic activity of Pt–Ru for methanol electro-oxidation depends on intimate contact between Pt and Ru, promoting higher mobility of CO from Pt to Ru and thus higher turnover rate.

This structure–performance correlation motivates the development of better routes for synthesizing Pt–Ru nanoparticles with controlled atom-scale architecture. Conventional wet impregnation and incipient wetness methods offer limited control over nanoparticle size. Moreover, these methods may produce particles with a distribution of compositions and do not guarantee intimate contact between the constituent metals. Molecular cluster compounds [such as [13,14] $PtRu_5(CO)_{16}$ and $Pt_2Ru_4(CO)_{16}$] provide better control over stoichiometry but only for limited Pt:Ru ratio values. A wide array of colloidal synthesis routes have also been explored [15–24]. A comprehensive review of PtRu

electrocatalysts for fuel cells has been published very recently [25].

In this work, we explore dendrimer-mediated synthesis of Pt–Ru catalysts for methanol electro-oxidation. Poly(amidoamine) (PAMAM) dendrimers feature interior amine and amide groups that can interact with metal ion precursors through coordination chemistry or ligand exchange reactions. This capability led directly to the use of PAMAM as a protecting ligand for the synthesis of PAMAM-stabilized metal nanoparticles [26–32] as well as supported metal catalysts [33,34]. The synthesis begins with the complexation of the metal precursor with PAMAM in aqueous solution. Appropriate dialysis procedures [35] can be used to remove unwanted chloride anions (from common precursors such as K_2PtCl_4, H_2PtCl_6 and $RuCl_3$) that might otherwise lead to catalyst poisoning [36–38]. Finally, the PAMAM–metal complex is deposited onto a porous catalyst support followed by reduction with H_2 gas at elevated temperature. Alternately, the complex solution can be treated first with a reducing agent ($NaBH_4$ or H_2 gas), followed by deposition onto the support.

We have a thorough understanding of the complexation of metal precursors with PAMAM, and our colleagues have employed PAMAM-mediated synthesis to prepare oxide-supported Ru catalysts [33,34]. Other groups have demonstrated the use of PAMAM to deliver metal complexes directly onto catalyst supports [39,40]. Building on this knowledge, this report describes our use of PAMAM-mediated synthesis to prepare carbon-supported Pt–Ru bimetallic catalysts. We also prepared conventional wet impregnation catalysts, identical except for their omission of PAMAM from the recipe. We have characterized the physical properties of both conventional and PAMAM-based Pt–Ru catalysts and have evaluated their performance for methanol electro-oxidation.

2. Experimental methods

2.1. Chemicals and materials

Hydroxyl-terminated poly(amidoamine) (PAMAM) dendrimer (generation 4, denoted as G4OH, 10 wt% in methanol), K_2PtCl_4 (99.99%), and $RuCl_3 \cdot zH_2O$ (99.98%) were purchased from Aldrich. All water was deionized to a resistivity of 18 MΩ-cm using a Nanopure system (Barnstead). High surface area carbon black (Vulcan XC-72R) served as the catalyst support. Commercial PtRu catalyst (C13–20, 20 wt% metal loading on Vulcan XC-72 carbon) was purchased from E-Tek, Inc. (www.etek-inc.com).

2.2. Synthesis of PAMAM–Pt–Ru complex

Our synthesis of the PAMAM–Pt–Ru complex involves sequential complexation of the Pt and Ru precursors with G4OH. We denote the complex as $G4OH-(Pt^{2+})_x(Ru^{3+})_y$ to indicate its nominal composition. To prepare $G4OH-(Pt^{2+})_{20}(Ru^{3+})_{20}$ complex, for example, we first dry a known mass of as-received G4OH solution (10 wt%) by rotary evaporation and/or impinging flow of dry N_2 gas, followed by dilution in DI water to 0.2 mM. We mix equal volumes of this stock G4OH solution and an aqueous 4.0 mM K_2PtCl_4 solution to yield $G4OH-(Pt^{2+})_{20}$ complex solution.

After stirring and aging for 3 days, the pH of the $G4OH-(Pt^{2+})_{20}$ complex solution decreases from 6.5 to 2.7. A previous study [41] suggests that the protonation of interior amine ($pK_a = 6.3$) groups at pH < 5 may prevent some ligand exchange reactions. After allowing 7 days for the formation of $G4OH-(Pt^{2+})_{20}$, we adjust the pH up to 7.0 by adding concentrated NaOH. Then we mix equal parts of $G4OH-(Pt^{2+})_{20}$ solution with an aqueous 2.0 mM $RuCl_3$ solution (anhydrous basis), yielding a 0.05 mM $G4OH-(Pt^{2+})_{20}(Ru^{3+})_{20}$ solution. We age the final solution for another 3 days prior to

Table 1
Metallic composition of $G4OH-Pt_xRu_y/C$ catalysts from atomic absorption spectroscopy.

Catalyst	Metal loading (wt%)[a]			Composition (x:y in Pt_xRu_y)	
	Pt	Ru	Total	Solution[a]	Final catalyst[b]
$G4OH-Pt_{40}/C$	20.1	0	20.1	40:0	40:0
$G4OH-Pt_{32}Ru_8/C$	21.9	1.72	23.6	32:8	34:6
$G4OH-Pt_{26}Ru_{14}/C$	17.5	3.54	21.1	26:14	28:12
$G4OH-Pt_{20}Ru_{20}/C$	12.3	5.5	17.8	20:20	22:18
$Pt_{20}Ru_{20}/C$ without G4OH	14.4	5.52	19.9	20:20	23:17
E-Tek PtRu	16.6	6.2	22.8	20:20	23:17

[a] Nominal values based on precursor concentrations prepared on an anhydrous basis.
[b] From atomic absorption spectroscopy.

catalyst preparation. In addition to $G4OH-(Pt^{2+})_{20}(Ru^{3+})_{20}$, we also prepared $G4OH-(Pt^{2+})_{26}(Ru^{3+})_{14}$, $G4OH-(Pt^{2+})_{32}(Ru^{3+})_8$, and $G4OH-(Pt^{2+})_{40}$ in the same way.

2.3. Catalyst preparation

To prepare catalysts, we dispersed known weights of carbon black powder in $G4OH-(Pt^{2+})_x(Ru^{3+})_y$ complex solution. All of the catalysts had a nominal, total metal loading of 20 wt% (the sum of Pt and Ru loadings) on the carbon black support. After sonication and 20 min of degassing with N_2, we sealed the suspensions and continued stirring for at least 24 h. We removed water by evaporation and rinsed the solid residue with ethanol. Finally, we dried the powder at 70 °C under vacuum. To reduce the metal species to zero valence, we heated the dried powders in H_2 gas at elevated temperature (typically 400 °C) for 2 h.

We denote the heat treated catalysts as $G4OH-Pt_xRu_y/C$. To determine the actual Pt and Ru loadings in the catalysts, we employed atomic absorption (AA) spectroscopy (Perkin Elmer Model 3300). The Pt-Ru/C samples were digested in aqua regia at 125 °C for 4 h. Carbon blanks and commercial samples of known Pt and Ru content were also analyzed. The resulting solutions were diluted with deionized water with lanthanum chloride added to enhance the Pt and Ru signals. Calibration standards were made from purchased 1.0 g/L Pt and Ru stock solutions and were verified by the use of check standards from an independent source. Sample sizes and dilution volumes of the digested samples were chosen so that expected results fell in the analytical ranges for Pt (up to 40 mg L^{-1}) and Ru (up to 20 mg L^{-1}).

Table 1 presents the catalysts prepared in this work. The final values of x and y in the $G4OH-Pt_xRu_y/C$ catalysts differ slightly from the precursor solution values due to the contribution of hydration from $RuCl_3 \cdot zH_2O$. In the following discussion, we routinely refer to the solution values of x and y in accord with usage in previous literature. The measured metal weight loadings and compositions can be found in Table 1.

To prepare each electrocatalyst electrode, we first prepared an "ink paste" by dispersing 8 mg of catalyst sample in 1.0 mL ethanol solution with ultrasonication for 30 min. Next, we coated 15 µL of ink paste (in three 5 µL aliquots) and 5 µL Nafion solution (5% in isopropyl alcohol) onto a glassy carbon disk, followed by drying in air for 30 min at 60 °C.

2.4. Material characterization

We monitored PAMAM–Pt–Ru complexation using a Shimadzu UV 2010 UV–vis spectrophotometer (UV–vis) with quartz cells of 10 mm path length. The background spectrum was subtracted by using an identical cell filled with deionized water.

We used transmission electron microscopy (TEM) to measure nanoparticle size. TEM samples were prepared by depositing

small drops of sonicated catalyst suspension in ethanol solutions (2.5 μM) onto standard carbon-coated copper TEM grids, followed by drying in air. TEM images were obtained using (typically) an operating voltage of 200 kV with a magnification of 300,000–500,000×. We estimated the average particle diameter by manual measurement of the size of at least 100 randomly selected particles in the TEM images.

X-ray diffraction (XRD) patterns were recorded using a Rigaku D/Max-2100 powder X-ray diffractometer with area detector using Cu Kα source ($\lambda = 1.54056$ nm) operating at 40 kV and 40 mA. The angular resolution in the 2θ-scans was 0.05°. Each full pattern was fit using Jade XRD software (version 7.5, Materials Data, Inc.) to determine peak locations, peak FWHMs, and crystallite diameters. Face centered cubic (fcc) lattice parameters (a) were calculated from the locations of the (2 2 0) peaks using the Scherrer equation [42,43].

We carried out X-ray photoelectron spectroscopy (XPS) experiments using a Kratos AXIS Ultra system with a base pressure of 10^{-9} Torr. The Al anode with focusing monochromator produces an Al Kα line with a width of <0.26 eV. Carbon-supported Pt–Ru catalysts were applied to one side of double-sided carbon conductive tape. The other side of the tape was adhered to a piece of Ta sheet. All samples were exposed to air during preparation and transfer to the XPS system. The samples were charge-compensated with the AXIS charge balance system that incorporates a magnetic immersion lens. The XPS spectra for C(1s), N(1s), Ru(3p), and Pt(4f) regions were averaged over four sweeps with a step size of 0.05 eV, a dwell time of 0.2 s, and a pass energy of 40 eV (except for Ru(3p), 160 eV). The peaks in the spectra were fit by using the shareware program XPSPEAK with Gaussian–Lorentzian peak shapes and a Shirley background.

2.5. Electrochemical characterization

Our cyclic voltammetry experiments employed a conventional electrochemical three-electrode test cell. A rotating disk electrode (RDE) with a glassy carbon disk (5 mm o.d.) served as the working electrode. Platinum wire and a standard Hg/HgSO4 (0.64 V vs. RHE) cell were used as the counter and reference electrodes, respectively.

All potentials in this work are quoted against reversible hydrogen electrode (RHE). We measured cyclic voltammogram (CV) curves at room temperature ($23 \pm 2 °C$) using an EG&G model 273 potentiostat/galvanostat. The sweep rate in the CV measurement was 20 mV s^{-1}. The upper potential of the cycle was limited to 1.1 V for Pt/C catalysts and 0.74 V for PtRu/C catalysts in order to avoid the loss of Ru as reported previously [44,45]. Methanol electro-oxidation experiments employed solutions containing 0.5 M CH3OH in 0.5 M H2SO4, prepared from high purity sulfuric acid, methanol, and double distilled water. All electrolyte solutions were purged by high purity N2 for 30 min prior to measurements. Data were collected over a minimum of five cycles with monitoring to assure reproducibility over successive cycles.

3. Results and discussion

3.1. Formation of G4OH–$(Pt^{2+})_x(Ru^{3+})_y$ bimetallic complexes

The complexation of the individual metals, Pt(II) [30,31] or Ru(III) [33,34], with PAMAM G4OH has been studied previously. Here, we study the formation of bimetallic G4OH–$(Pt^{2+})_x(Ru^{3+})_y$ complexes prepared by sequentially adding K2PtCl4 and RuCl3 to aqueous G4OH solutions.

Before considering G4OH–$(Pt^{2+})_x(Ru^{3+})_y$ complexes, it is instructive to examine G4OH–$(Ru^{3+})_y$ complexation. The UV–vis spectrum of a fresh solution of RuCl3 in pure water (Fig. 1) has char-

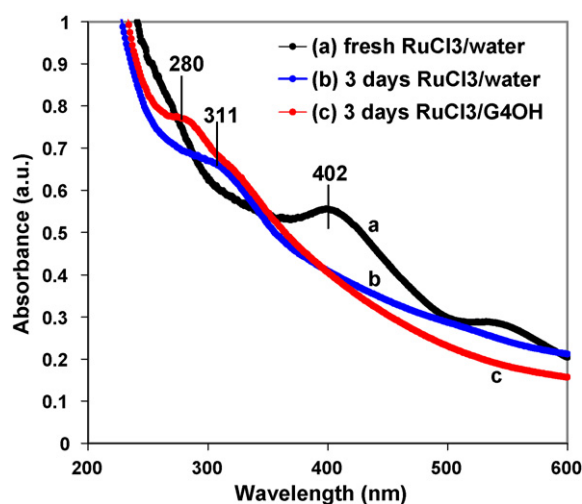**Fig. 1.** UV–vis spectra of RuCl3 solutions: (a) fresh RuCl3 in water; (b) RuCl3 in water after 3 days; and (c) RuCl3 in aqueous G4OH [nominally G4OH–$(Ru^{3+})_{20}$] aged 3 days.

acteristic peak at 402 nm. Over time, RuCl3 in pure water forms aqua complexes [46], manifested in the UV–vis spectrum as the disappearance of the 402 nm peak and the appearance of a peak at 311 nm. For RuCl3 in aqueous G4OH aged 3 days, the spectrum has a characteristic peak at 280 nm, ascribed previously to Ru–amine complexes [34]. From this, we infer that the absence of the peak at 311 nm implies preferential formation of G4OH–$(Ru^{3+})_y$ complexes rather than Ru aqua complexes.

Fig. 2 shows a series of UV–vis spectra during the steps leading to G4OH–$(Pt^{2+})_{20}(Ru^{3+})_{20}$. After mixing aged K2PtCl4 solution with G4OH solution, the appearance of the ligand-to-metal charge transfer (LMCT) band at 250 nm indicates the slow formation of the G4OH–$(Pt^{2+})_{20}$ complex (Fig. 2, curves a and b). After addition of RuCl3 to aqueous G4OH–$(Pt^{2+})_{20}$, the spectrum (Fig. 2, curve c) displays a weak peak at 402 nm and a broad absorbance over the 300–600 nm range as expected for RuCl3 in water. The persistence of the intense LMCT band at 250 nm (Fig. 2, curves c & d) indicates that Pt^{2+} remains complexed with G4OH. The intensity of the 402 nm peak decreases slowly over time (Fig. 2, curve d), consistent with the formation of Ru complexes. The absence of a
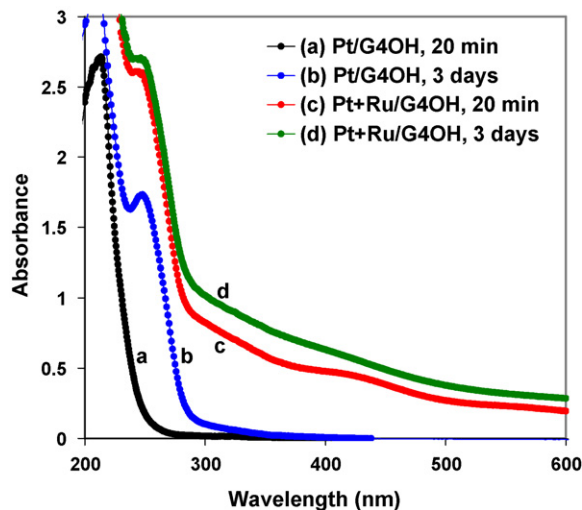

Fig. 2. UV–vis spectra at various stages during the formation of G4OH–$(Pt^{2+})_{20}(Ru^{3+})_{20}$ complex: (a) 20 min after mixing aged K2PtCl4 and G4OH solutions; (b) G4OH–$(Pt^{2+})_{20}$ after 3 days; (c) 20 min after mixing RuCl3 and G4OH–$(Pt^{2+})_{20}$ solutions; and (d) G4OH–$(Pt^{2+})_{20}(Ru^{3+})_{20}$ solution aged 3 days.

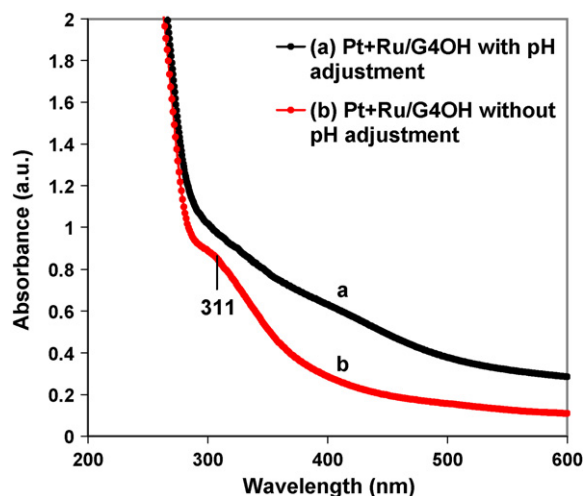**Fig. 3.** UV–vis spectra of G4OH–$(Pt^{2+})_{20}(Ru^{3+})_{20}$ complex solutions: (a) with adjustment of G4OH–$(Pt^{2+})_{20}$ solution to pH 7.0 before addition of $RuCl_3$; and (b) no pH adjustment before addition of $RuCl_3$.

peak at 311 nm implies that Ru^{3+} has complexed with G4OH preferentially over water. However, the strong Pt–G4OH LMCT band at 250 nm makes it difficult to detect any peak near 280 nm arising from Ru–G4OH complexation.

Another experiment supports the view that Ru^{3+} has complexed with G4OH–$(Pt^{2+})_{20}$ to form G4OH–$(Pt^{2+})_{20}(Ru^{3+})_{20}$. Fig. 3 compares the UV–vis spectra of G4OH–$(Pt^{2+})_{20}(Ru^{3+})_{20}$ solutions with and without adjustment of the G4OH–$(Pt^{2+})_{20}$ solution from pH 2.7–7.0 prior to the addition of $RuCl_3$. Without pH pre-adjustment (Fig. 3, curve b), the spectrum of G4OH–$(Pt^{2+})_{20}(Ru^{3+})_{20}$ manifests a distinct peak around 311 nm, similar to that seen for $RuCl_3$ in pure water (Fig. 1, curve a). This implies that Ru^{3+} has preferentially complexed with water rather than G4OH in this solution. This is consistent with previous work [41] indicating that at low solution pH, protonation of PAMAM's amine and amide groups may prevent Ru^{3+} complexation with PAMAM. The absence of the 311 nm peak in pH-adjusted G4OH–$(Pt^{2+})_{20}(Ru^{3+})_{20}$ solution (Fig. 3, curve a) supports the assertion that Ru^{3+} has complexed with G4OH–$(Pt^{2+})_{20}$ to form G4OH–$(Pt^{2+})_{20}(Ru^{3+})_{20}$. We conclude that sequential complexation Pt^{2+} and Ru^{3+} with G4OH dendrimer produces an aqueous, bimetallic solution complex, here denoted as G4OH–$(Pt^{2+})_x(Ru^{3+})_y$.

3.2. Catalyst physical characterization

3.2.1. Composition and metal loading

G4OH–Pt_xRu_y/C catalysts were prepared by impregnating high surface area carbon with G4OH–$(Pt^{2+})_x(Ru^{3+})_y$ complexes, followed by thermal treatment in H_2 for 2 h to reduce the metal species and remove G4OH dendrimer. The actual metal loading and Pt:Ru ratio were determined by AA spectroscopy (Table 1). The Pt:Ru ratios measured by AA are slightly lower than the nominal values based on the precursor solution concentrations, similar to that reported previously [47]. This is due to the water content in $RuCl_3 \cdot zH_2O$; its precursor solution was prepared on an anhydrous basis. Based on the AA results, we estimate that $z \sim 2$. In accord with previous literature, we refer to the nominal x and y values in "G4OH–Pt_xRu_y/C" for convenience.

3.2.2. Chemical state after activation

Catalyst activation entails H_2 treatment at elevated temperature to decompose the PAMAM and reduce the metals. The optimal temperature maximizes PAMAM decomposition while minimiz-

ing catalyst sintering. X-ray photoelectron spectroscopy (XPS) was used to characterize the products of PAMAM decomposition and measure metal valences in the catalysts after H_2 activation at different temperatures.

Fig. 4 shows the N(1s) region of the XPS spectra for G4OH–$Pt_{20}Ru_{20}$/C catalysts treated in H_2 at various temperatures. For the catalyst at room temperature, the spectrum can be fit with two main peaks at 399.5 and 400.4 eV as well as a smaller feature at 402.0 eV. The 400.4 and 402.0 eV peaks are assigned to amine and amide nitrogens, respectively. Although these binding energies are ~1 eV higher than those typically observed in amines and amides [48,49], they are consistent with the N(1s) binding energies previously reported for G4OH and Pt–G4OH films on Au-coated Ta [50]. The high binding energy 402.0 eV peak cannot be attributed to nitrogens coordinated with the metal ions because this feature was also observed for the G4OH in the absence of the metal ions. Furthermore, the amide:amine peak intensity ratio is much lower than 2:1 value expected based on the dendrimer stoichiometry, also in agreement with the previous studies of the G4OH dendrimer films [50]; the signal from the amide nitrogens is apparently screened compared to that of the amine nitrogens.

The peak at 399.5 eV is attributed surface species resulting from C–N bond scission in the dendrimer. This decomposition product is related to the presence of the metal ions, given that the 399.5 eV peak does not appear in the spectrum of G4OH films but is present in Pt–G4OH films at room temperature [50]. After H_2 activation at 200 °C, the integrated nitrogen signal decreases by 50% as nitrogen-containing species desorb from the surface, and the 399.5 eV peak from the decomposition species becomes the dominant feature in the spectrum. A small low binding energy peak at 398.1 also appears and could be assigned to atomic nitrogen on zero-valent metal sur-
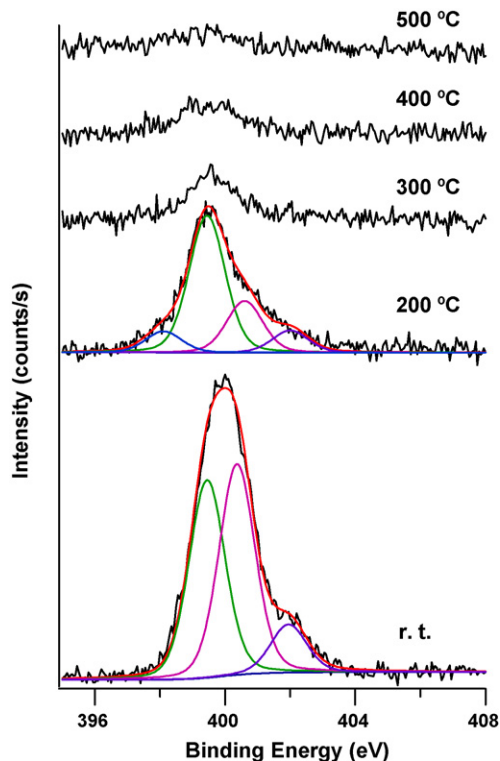

Fig. 4. X-ray photoelectron spectra in the N(1s) region for G4OH–$Pt_{20}Ru_{20}$/C catalysts treated with H_2 for 2 h at the indicated temperatures (curves shifted vertically for clarity). The "r.t." denotes the catalyst treated with H_2 for 2 h at room temperature. The r.t. and 200 °C sets include the original spectrum as well as the fitted spectrum (including fitted baseline and individual deconvoluted peaks with FWHM values of 1.3 eV).
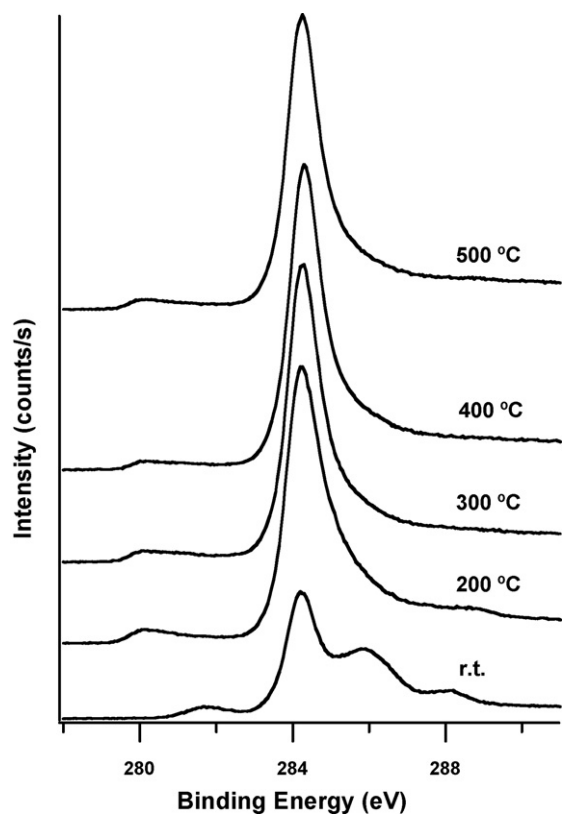
from the surface, based on the substantial increase in carbon signal at 284.3 eV due to the carbon support.

Treatment with H_2 gas is intended to reduce the Pt and Ru valence, ideally to the zero-valent metallic state. XPS data (supporting information, Fig. S1) for the G4OH–$Pt_{20}Ru_{20}$/C sample before treatment shows that the Pt(4f) region can be fit with a single Pt(4f) doublet with Pt($4f_{7/2}$) and Pt($4f_{5/2}$) binding energies of 72.9 and 76.2 eV, respectively; in all spectra, the Pt(4f) doublet was fit by fixing the binding energy splitting at 3.35 eV, fixing the $4f_{7/2}$ to $4f_{5/2}$ peak area ratio at 4:3 and keeping the FWHM values the same for both peaks (Fig. S1). The Pt($4f_{7/2}$) binding energy of 72.8 eV is consistent with that expected for Pt^{+2} [53–55]. After reduction at 200 °C, there is a significant shift to lower binding energies, and the spectrum is fit with two Pt(4f) doublets with $4f_{7/2}$ binding energies of 72.7 and 71.3 eV and a peak area ratio of 30:70. The higher binding energy feature is again attributed to Pt^{+2} while the lower binding energy peak is assigned to metallic Pt [56]. Heating in H_2 at 200 °C causes reduction of Pt^{+2} to Pt^0 as expected, but either the Pt was not completely reduced, or Pt became reoxidized upon transfer in air to the XPS chamber. Reduction at higher temperatures does not significantly change the Pt(4f) peak shape, although the signal intensity decreases by 16% between the 200 and 500 °C reduction treatments, presumably due to sintering of the Pt particles.

Fig. 6 shows the Ru($3p_{3/2}$) region of the XPS spectra for G4OH–$Pt_{20}Ru_{20}$/C treated in H_2 at various temperatures. For room temperature sample, the Ru($3p_{3/2}$) spectrum is fit with two peaks at 463.4 and 466.5 eV, assigned to Ru^{+4} [57,58] and Ru^{+6} [57] in RuO_2 and RuO_3, respectively. The large FWHM (3.5 eV) for these peaks suggests that other oxidation states for Ru could be present. However, a previous study [57] of carbon-supported Pt–Ru particles also reported peak widths on the order of 4 eV for a Ru(3p) spectrum
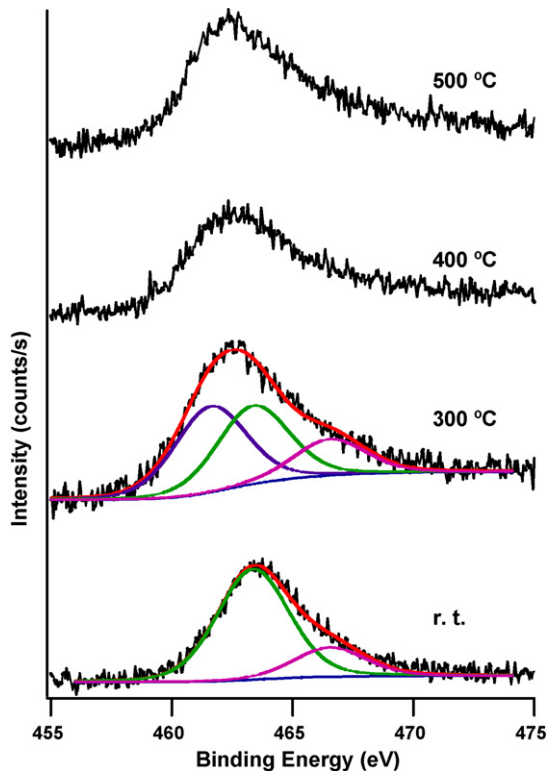
Fig. 5. X-ray photoelectron spectra in the C(1s) region for G4OH–$Pt_{20}Ru_{20}$/C catalysts activated with H_2 for 2 h at the indicated temperatures (curves shifted vertically for clarity). The "r.t." curve is for G4OH–$Pt_{20}Ru_{20}$/C catalyst treated with H_2 for 2 h at room temperature.

faces [51]. The nitrogen signal continues to decrease to 13% of the room temperature value after reduction at 300 °C and drops almost to zero after reduction at 500 °C.

The C(1s) region of the XPS spectra (Fig. 5) for G4OH–$Pt_{20}Ru_{20}$/C treated with H_2 at room temperature is complicated because the dendrimer itself contains a number of chemically different carbons. At all temperatures, the dominant feature in the spectrum is the 284.3 eV peak from the carbon support. Small peaks are observed in the 280–282 eV region from the Ru(3d) signal, as will be discussed below. In the room temperature spectrum, the highest binding energy peak at 288.3 eV is assigned to carbonyl carbons, and the broad peak centered at 285.9 eV corresponds to C–OH, C–N (amine) and C–N (amide) species, as previously observed for G4OH films [48,52]. There should also be contribution from aliphatic carbons around 285.7 eV, but this peak overlaps with the high intensity feature from the carbon support.

Following reduction at 200 °C, the intensities of the 288.3 eV and 285.9 eV peaks approach zero, indicating that almost all C=O, C–O and C–N bonds are broken. Furthermore, the total carbon signal intensity increases by ∼75%, with most of the intensity occurring at 284.3 eV. This demonstrates removal of most of the carbon-containing species from the surface, allowing greater X-ray penetration to the underlying carbon support and thus an increase in that peak. Reduction at 300 °C results in a minor increase in the carbon signal at 284.3 eV and the complete disappearance of the 288.5 and 285.9 eV peaks. There are no further changes upon reduction at higher temperatures. It is impossible to determine if all of the carbon-containing species are removed from the surface during reduction because the carbon support signal appears at the same binding energy as CH_x [52]. However, it is clear that a large fraction of the residual carbon from dendrimer decomposition is removed

Fig. 6. X-ray photoelectron spectra in the Ru($3p_{3/2}$) region for G4OH–$Pt_{20}Ru_{20}$/C catalysts treated with H_2 for 2 h at the indicated temperatures (curves shifted vertically for clarity). The "r.t." set of curves is for G4OH–$Pt_{20}Ru_{20}$/C catalyst treated with H_2 for 2 h at room temperature. The "r.t." and 300 °C sets include the original spectrum, the fitted spectrum, the fitted baseline and deconvoluted peaks with FWHM values of 3.5 eV.

Table 2
Summary of TEM and XRD results for G4OH–Pt$_x$Ru$_y$/C catalysts.

Catalyst	Activation temperature (°C)	TEM		XRD		Vegard's Law[b]
		$d_{TEM} \pm \sigma_{TEM}$ (nm)	COV[a] (%)	d_{XRD} (nm)	a_{fcc} (Å)	a_{Vegard} (Å)
G4OH–Pt$_{20}$Ru$_{20}$/C	300	3.2 ± 0.6	19	3.4 ± 0.5	3.8820 ± 0.0126	3.8583
G4OH–Pt$_{20}$Ru$_{20}$/C	400	3.9 ± 0.7	18	3.2 ± 0.3	3.8833 ± 0.0091	3.8583
G4OH–Pt$_{20}$Ru$_{20}$/C	500	4.9 ± 0.9	18	3.4 ± 0.3	3.8869 ± 0.0082	3.8583
G4OH–Pt$_{40}$/C	400	5.1 ± 1.2	24	6.4 ± 0.5	3.9203 ± 0.0029	–
G4OH–Pt$_{32}$Ru$_8$/C	400	4.7 ± 1.2	26	4.0 ± 0.3	3.8921 ± 0.0037	3.8955
G4OH–Pt$_{26}$Ru$_{14}$/C	400	4.4 ± 0.7	16	3.9 ± 0.3	3.8923 ± 0.0064	3.8769
G4OH–Pt$_{20}$Ru$_{20}$/C	400	3.9 ± 0.7	18	3.2 ± 0.3	3.8833 ± 0.0091	3.8583
Pt$_{20}$Ru$_{20}$/C without G4OH	400	7.4 ± 3.7	50	10.2 ± 0.7	3.8988 ± 0.0017	3.8583

[a] Coefficient of variation (COV) = d_{TEM}/σ_{TEM}.

[b] Lattice parameters calculated from the nominal Ru mole fraction (x_{RU}) using Vegard's Law, $a_{Vegard} = a_{fcc,Pt/C} - kx_{Ru}$, with $a_{fcc,Pt/C}$ = 3.9203 Å and k = 0.124 Å.

attributed to a mix of RuO$_2$ and RuO$_3$. After treating in H$_2$ at 300 °C, we see a shift to lower binding energy, indicating that the metal is reduced. The 300 °C spectrum is fit with peaks at 463.4 and 466.5 eV from the Ru oxides, as well as a peak at 461.6 eV assigned to metallic Ru [59,60]. No additional shifts in binding energy are observed after reduction at higher temperatures. Thus, H$_2$ treatment at elevated temperatures cannot fully reduce the Ru, or fully reduced Ru undergoes partial re-oxidation upon exposure to ambient O$_2$.

Although the Ru(3d) peaks (Fig. 5) have much higher intensity than Ru(3p) peaks, the Ru(3d) region overlaps with the very intense C(1s) peaks from the carbon support. Although Ru(3d) region cannot be fit, the data indicate the presence of ruthenium oxides before

treatment and a reduced form of Ru after H$_2$ treatment at 200 °C and higher (Fig. 5). The Ru(3d$_{5/2}$) peak centered at 281.8 eV before treatment is consistent with the presence of RuO$_2$ at 280.6–281.0 eV [61–63] and RuO$_3$ at 282.5–283.0 eV [62]. Furthermore, the shift in Ru(3d$_{5/2}$) binding energy to 280.2 eV after treatment suggests [56] the formation of metallic Ru.

The Ru(3p$_{3/2}$) region of the XPS spectra clearly indicate the presence of reduced, zero-valent Ru in the G4OH–Pt$_{20}$Ru$_{20}$/C catalysts. A plausible speculation [64] is that the surface Ru atoms may be +4 or +6 valence and exist in the form of oxides, while interior Ru atoms may be zero-valent and alloyed with Pt^0. The testing of this hypothesis, as well as proof that G4OH–Pt$_x$Ru$_y$ nanoparticles are
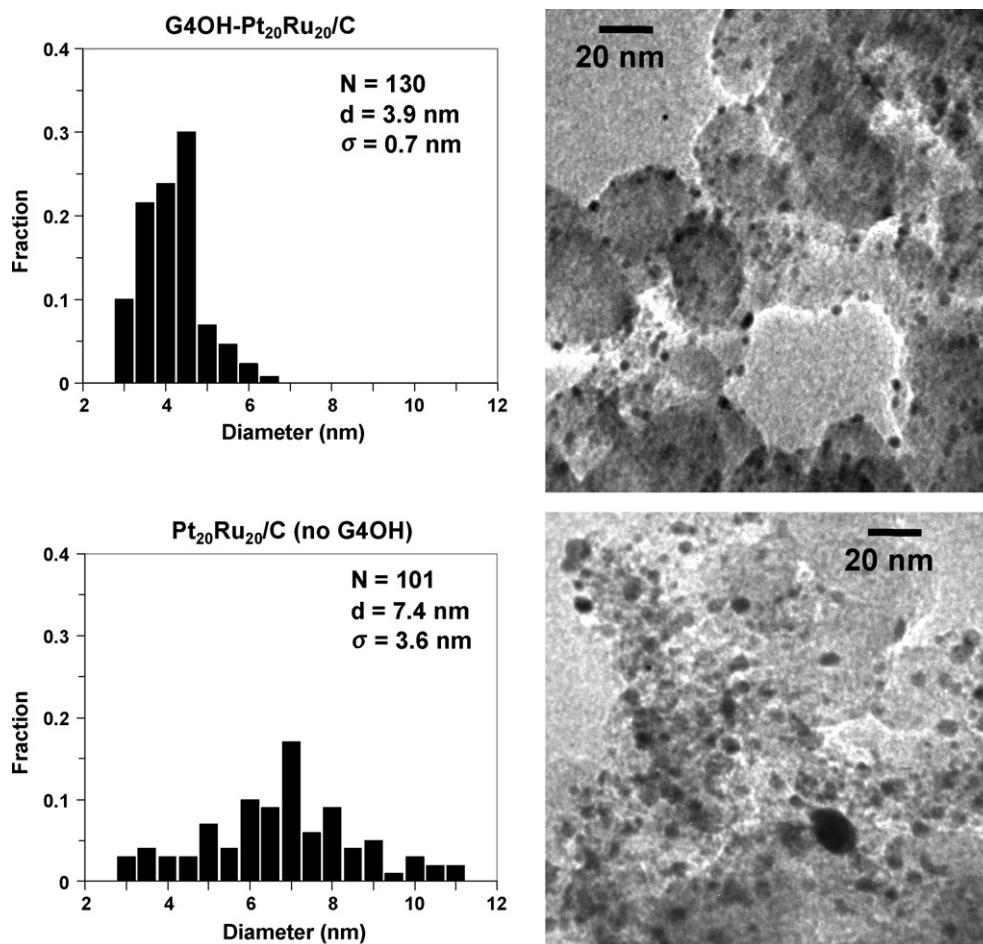

Fig. 7. Particle size distributions and TEM images for (top) G4OH–Pt$_{20}$Ru$_{20}$/C and (bottom) conventional Pt$_{20}$Ru$_{20}$/C made without G4OH. The catalysts were activated under H$_2$ at 400 °C for 2 h.
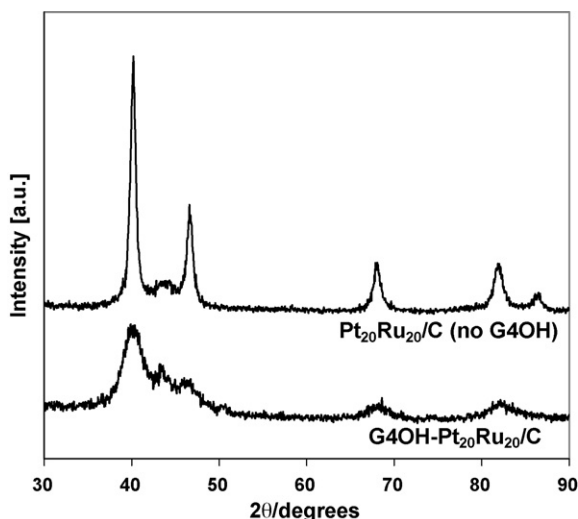
Fig. 8. X-ray diffraction patterns of G4OH–$Pt_{20}Ru_{20}$/C catalyst as well as $Pt_{20}Ru_{20}$/C catalyst made without G4OH. Both catalysts were activated in H_2 at 400 °C for 2 h.

truly bimetallic alloys, are addressed in a forthcoming report that includes characterization of G4OH–Pt_xRu_y nanoparticles by X-ray absorption spectroscopy [65].

3.2.3. Particle size and crystal structure

Metal particle sizes were characterized by TEM. Fig. 7 (top) shows a typical TEM image of the G4OH–$Pt_{20}Ru_{20}$/C catalyst after H_2 treatment at 400 °C. This image shows uniform, well-dispersed particles. The particle size distribution indicates an average diameter of 3.9 ± 0.7 nm (standard deviation). Fig. 7 (bottom) shows a typical TEM image and corresponding particle size distribution for a "conventional" $Pt_{20}Ru_{20}$/C catalyst made without added G4OH. The metal particles in the conventional $Pt_{20}Ru_{20}$/C catalyst have an average diameter of 7.4 ± 3.7 nm. Under preparation conditions identical in all respects except for the presence of G4OH in the recipe, G4OH–$Pt_{20}Ru_{20}$/C catalyst contains metal particles that are 50% smaller (on average) than those in the conventional $Pt_{20}Ru_{20}$/C catalyst. Moreover, use of G4OH in the recipe leads to a much more narrow particle size distribution.

Typical TEM images and particle size distributions for all of the G4OH–Pt_xRu_y/C catalysts are shown in the Supporting Information section (Fig. S2), and the results are summarized in Table 2. For G4OH–$Pt_{20}Ru_{20}$/C catalysts treated at temperatures increasing from 300 to 500 °C, d_{TEM} increased from 3.2 ± 0.6 to 4.9 ± 0.9 nm. This increase may be due to particle sintering as might be expected at elevated temperatures. For all other catalysts, an activation temperature of 400 °C was employed in order to ensure complete G4OH decomposition while avoiding excessive particle sintering.

X-ray diffraction (XRD) reveals the crystal structure and size of the metal particles in our supported catalysts; Figs. 8 and 9 show XRD patterns, and Table 2 summarizes the results. The XRD patterns for all of the catalysts are generally consistent with fcc crystallites with peaks readily indexed to the Pt (1 1 1), (2 0 0), (2 2 0), (3 1 1), and (2 2 2) faces. For catalysts containing Ru, all of the peaks are shifted to higher 2θ values than expected for pure Pt. In quantitative terms, the fcc lattice parameter values (Table 2) for catalysts containing Ru are all significantly lower than that of the G4OH–Pt_{40}/C catalyst or published values for bulk Pt [43]. These observations are consistent with substitution of Ru atoms in the Pt fcc structure to form bimetallic alloys [43,47,57,66].

Fig. 8 shows XRD patterns for the G4OH–$Pt_{20}Ru_{20}$/C catalyst as well as the $Pt_{20}Ru_{20}$/C catalyst prepared without G4OH. The peaks in the $Pt_{20}Ru_{20}$/C pattern are noticeably

sharper, indicating larger, more crystalline metal particles in $Pt_{20}Ru_{20}$/C ($d_{XRD} = 10.2 \pm 0.7$ nm) than in the G4OH–$Pt_{20}Ru_{20}$/C ($d_{XRD} = 3.2 \pm 0.3$ nm). This finding corroborates the TEM results: the use of G4OH in the recipe leads to much smaller metal particles.

Lattice parameters for both of these catalysts indicate the formation of Pt–Ru alloys. However, both patterns also show a distinct peak near $2\theta = 44°$ which has previously been indexed as hexagonally close-packed (hcp) Ru [67]. Any other hcp Ru peaks in the pattern would overlap with those of fcc Pt [67], so we have not attempted to discriminate between Pt and Ru in peak fitting. Regardless, these patterns show that Pt–Ru alloy particles predominate in $Pt_{20}Ru_{20}$/C prepared with and without G4OH, but some of the Ru in these samples may exist in the hcp form, possibly as Ru-rich alloys with Pt [66].

Fig. 9 shows XRD patterns of G4OH–Pt_xRu_y/C catalysts with nominal Ru content ranging from 0 to 50 mol%. With increasing Ru content, the peaks broaden and synchronously shift toward higher angles consistent with substitution of Ru atoms for Pt in the fcc lattice. This is most clearly seen in the (2 2 0) peak around $2\theta = 68°$. The peak shifts result in smaller lattice parameters (a_{fcc}) relative to pure Pt (Table 2; also Apendix Bsee Fig. S3, Supporting Information), indicating alloying of Ru with Pt. The particle size d_{XRD} calculated by the Debye–Scherrer equation [42] (Table 2) is greatest for G4OH–Pt_{40}/C and decreases with increasing Ru content, following the same trend as seen in d_{TEM}. These observations indicate that all of the G4OH–Pt_xRu_y/C catalysts are Pt–Ru alloys [43,47] with Ru incorporation increasing with nominal Ru content.

The G4OH–$Pt_{20}Ru_{20}$/C catalyst (Fig. 9) is the only one that shows clear evidence of a peak at $2\theta = 44°$, indicative of some Ru not incorporated in the Pt fcc lattice. Table 2 and Fig. S3 also show lattice parameter values calculated from Vegard's Law [68] based on the nominal Ru mole fraction [$y/(x + y)$]. Vegard's Law predicts a_{fcc} well for $y = 8$, but a_{fcc} is above the theoretical value for $y = 14$ and 20. This provides evidence that not all of the Ru is alloyed with Pt for higher Ru contents. Alternately, the possibility exists that Vegard's Law may not be accurate for such small particles.

The value of a_{fcc} for $Pt_{20}Ru_{20}$/C prepared without G4OH (Table 2; Fig. S3) is even higher than that of G4OH–$Pt_{20}Ru_{20}$/C. This suggests the intriguing possibility that G4OH helps to promote Pt–Ru alloying, or helps prevent Pt–Ru segregation during catalyst activation, at least for 1:1 Pt:Ru ratio.
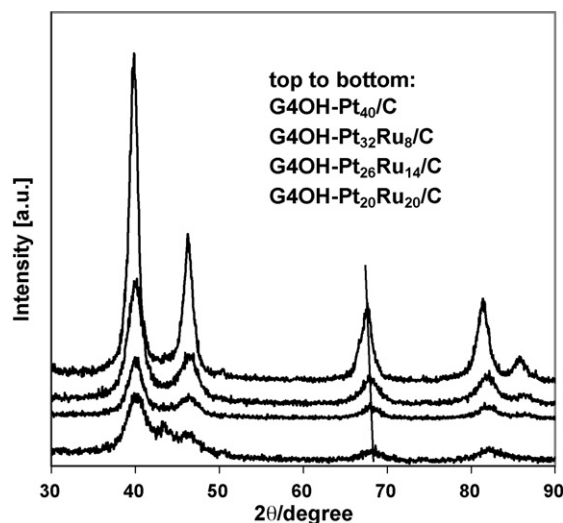

Fig. 9. X-ray diffraction patterns of G4OH–Pt_xRu_y/C catalysts with different Pt:Ru ratios. Top to bottom: G4OH–Pt_{40}/C; G4OH–$Pt_{32}Ru_8$/C; G4OH–$Pt_{26}Ru_{14}$/C; and G4OH–$Pt_{20}Ru_{20}$/C. The line near 68° guides the eye with regard to the shift of the Pt (2 2 0) peak. All catalysts were activated in H_2 at 400 °C for 2 h.

Table 3
Summary of CV results for methanol electro-oxidation by various Pt_xRu_y/C catalysts.

Catalyst	Activation temperature (°C)	Current density (mA mg^{-1}-Pt)[a]	
		At 0.3 V	At 0.7 V
G4OH–$Pt_{20}Ru_{20}$/C	300	17.7 ± 0.1	159 ± 1.0
G4OH–$Pt_{20}Ru_{20}$/C	400	13.6 ± 4.6	210 ± 21
G4OH–$Pt_{20}Ru_{20}$/C	500	17.8 ± 2.5	204 ± 22
G4OH–Pt_{40}/C	400	5.8 ± 0.6	64.4 ± 11.3
G4OH–$Pt_{32}Ru_8$/C	400	2.9 ± 0.3	79.8 ± 6.1
G4OH–$Pt_{26}Ru_{14}$/C	400	4.6 ± 0.1	92.7 ± 8.4
G4OH–$Pt_{20}Ru_{20}$/C	400	13.6 ± 4.6	210 ± 21
E-Tek PtRu/C	n.a.	6.4 ± 0.2	130 ± 12.0
$Pt_{20}Ru_{20}$/C without G4OH	400	3.3 ± 0.1	13.6 ± 0.2

[a] Averages based on three independent experiments, except for the $Pt_{20}Ru_{20}$/C (no G4OH) which was measured twice.

For G4OH–$Pt_{20}Ru_{20}$/C catalysts activated with H_2 at different temperatures, XRD results do not indicate a significant variation of particle size (Table 2). This observation is in contrast with the TEM results which indicate an increase in particle size with activation temperature. This might be due to differences in sampling biases inherent in the two methods. Likewise, XRD does not indicate a significant variation of lattice parameter with activation temperature. Nonetheless, the lattice parameter for all of the G4OH–$Pt_{20}Ru_{20}$/C catalysts is significantly lower than that of the G4OH–Pt_{40}/C catalyst or bulk Pt [43]. This is an unambiguous indication of the formation of Pt–Ru alloys in the G4OH–$Pt_{20}Ru_{20}$/C catalysts.

3.3. Electrocatalytic characterization

3.3.1. Activation temperature

Activation of G4OH–Pt_xRu_y/C catalysts requires elevated temperatures for H_2 reduction of the metals as well as decomposition and removal of G4OH. However, elevated temperatures may also lead to particle sintering as indicated by TEM results. To see if there is an optimal activation temperature, we measured cyclic voltammograms (CVs) for G4OH–$Pt_{20}Ru_{20}$/C catalysts activated at varying temperatures. Table 3 shows average values of the current density (normalized by the Pt weight loading) for methanol electro-oxidation by all of the tested catalysts at 0.3 and 0.7 V. For the G4OH–$Pt_{20}Ru_{20}$/C catalysts activated at varying temperatures, the current density at 0.7 V provides a relative indication of activity for MeOH oxidation. The G4OH–$Pt_{20}Ru_{20}$/C catalysts activated at 400 and 500 °C have about the same catalytic activity, significantly higher than that for G4OH–$Pt_{20}Ru_{20}$/C catalyst activated at 300 °C. We selected 400 °C as the standard activation temperature for all other G4OH–Pt_xRu_y/C catalysts. Although we do not know if 400 °C is optimal, it leads to maximal activity while minimizing the risk of nanoparticle sintering.

3.3.2. Catalyst composition

Structural characterization of G4OH–Pt_xRu_y/C catalysts shows that with increasing Ru content, the metal nanoparticle size decreases, Pt–Ru alloying increases, and crystallographic features associated with hcp ordering of Ru appear (Fig. 9). The electrocatalytic properties also show consistent trends with changes in Pt:Ru ratio.

Fig. 10 shows CV results for G4OH–Pt_xRu_y/C catalysts cycled in 0.5 M H_2SO_4 solution. This figure reports current density on an electrode area basis so that one can more clearly see the composition dependence of the current in the Pt–H oxidation region at low potential. For the G4OH–Pt_{40}/C catalyst, the CV curve has multiple peaks between 0.05 and 0.25 V due to Pt–H oxidation on
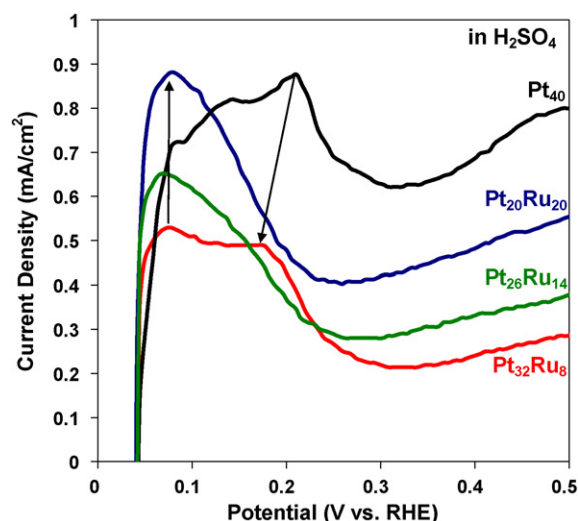

Fig. 10. Current density (mA cm^{-2}) vs. potential for G4OH–Pt_xRu_y/C catalysts in 0.5 M H_2SO_4 (from CV, sweep rate 20 mV s^{-1}). Catalyst compositions as indicated in the figure. Arrows are explained in the text.

different Pt crystallographic faces. Comparing G4OH–Pt_{40}/C with G4OH–$Pt_{32}Ru_8$/C catalyst, the dominant Pt–H oxidation peak at about 0.20 V for G4OH–Pt_{40}/C is shifted and greatly reduced in G4OH–$Pt_{32}Ru_8$/C (downward arrow in Fig. 10). With increasing Ru content, the Pt–H oxidation peak at 0.20 V disappears, and a new Pt–H oxidation peak appears and grows at about 0.075 V (upward arrow in Fig. 10). These observations signify modification of the Pt crystallite structure due to Pt–Ru alloying and, perhaps, preferential decoration of certain crystal faces by Ru and its oxides.

Significant variations in the location and shape of Pt–H oxidation peaks at low potential are also observed in 0.5 M H_2SO_4 solutions containing 0.5 M MeOH (Fig. 11, inset). Varying Ru content also presumably affects the current density in the range expected for double layer charging (0.3–0.6 V). These multiple, qualitative changes in the CV curves make it difficult to identify the onset potential for MeOH oxidation in a quantitative, rational way. Setting an arbitrary current density threshold [47] to identify onset potential is also potentially misleading. For these reasons, we use the value of
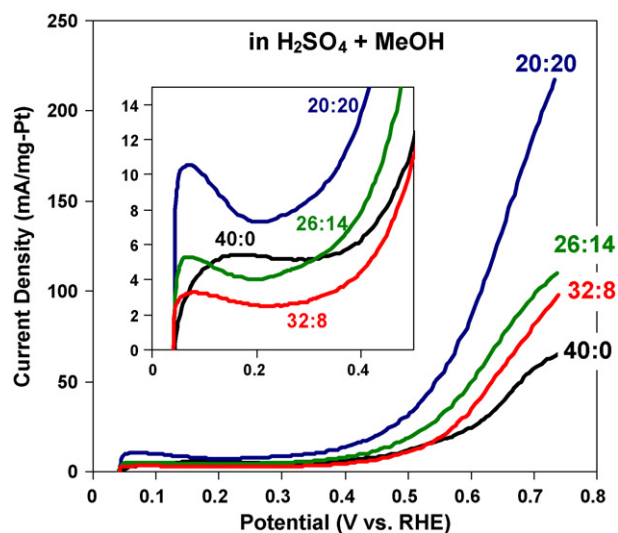

Fig. 11. Current density (mA mg^{-1}-Pt) vs. potential for methanol electro-oxidation by G4OH–Pt_xRu_y/C catalysts (from CV in 0.5 M H_2SO_4 + 0.5 M MeOH, sweep rate 20 mV s^{-1}). Values of x:y in G4OH–Pt_xRu_y/C are indicated in the figure. The inset shows the low voltage region.
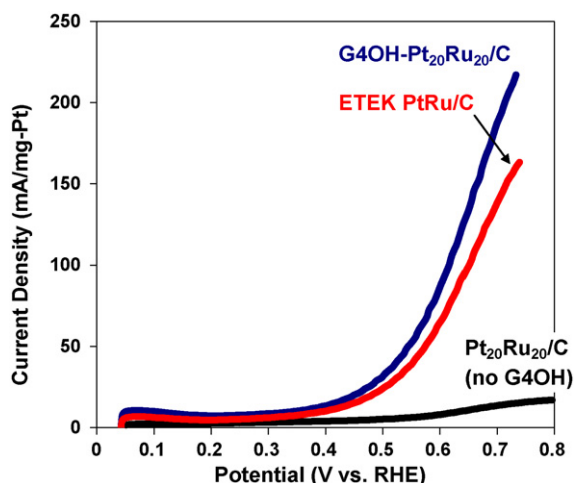
Fig. 12. Current density $(\text{mA mg}^{-1}\text{-Pt})$ vs. potential for methanol electro-oxidation by various PtRu/C catalysts, all with nominal 50:50 mole% Pt:Ru (from CV in 0.5 M H_2SO_4 + 0.5 M MeOH, sweep rate 20 mV s^{-1}).

the current density at 0.3 V vs. RHE, normalized by Pt mass (Table 3) as the basis for comparing the onset of MeOH oxidation by different catalysts.

Fig. 11 shows the cathodic polarization portions of the CV curves for MeOH oxidation by G4OH–Pt$_x$Ru$_y$/C catalysts, and Table 3 presents average current densities at 0.30 and 0.70 V. These data indicate that the catalytic activity, per unit mass of Pt, increases significantly with Ru content and is greatest for the G4OH–Pt$_{20}$Ru$_{20}$/C catalyst. Although we do not know if $x = y$ is optimal for maximum activity of G4OH–Pt$_x$Ru$_y$/C catalysts, it would be consistent with the optimal 1:1 Pt:Ru ratio found in previous studies [47] and commercial PtRu catalysts. Also, using the current density at 0.30 V as an indicator for the onset of MeOH oxidation, the G4OH–Pt$_{20}$Ru$_{20}$/C catalyst has the highest value and thus the earliest onset for MeOH oxidation.

Finally, we compare the performance of the G4OH–Pt$_{20}$Ru$_{20}$/C catalyst with a commercial PtRu/C catalyst (E-Tek, Inc.) as well as Pt$_{20}$Ru$_{20}$/C catalyst prepared identically except with G4OH omitted from the recipe (Fig. 12, Table 3). Clearly the Pt$_{20}$Ru$_{20}$/C catalyst prepared without G4OH has very low catalytic activity for MeOH oxidation. This demonstrates that the presence of the G4OH dendrimer in the recipe is critical to the formation of small PtRu nanoparticles with narrow particle size distribution, controlled composition, and high catalytic activity. Comparing the G4OH–Pt$_{20}$Ru$_{20}$/C catalyst with the commercial E-Tek catalyst, MeOH oxidation activity of the G4OH–Pt$_{20}$Ru$_{20}$/C catalyst is more than 60% higher than that of the E-Tek catalyst at a potential of 0.70 V (vs. RHE). Moreover, the G4OH–Pt$_{20}$Ru$_{20}$/C catalyst has higher activity at a potential of 0.30 V, suggesting earlier onset of MeOH oxidation during cathodic polarization.

4. Conclusions

This work has shown that PAMAM-based bimetallic G4OH–(Pt^{2+})$_x$(Ru^{3+})$_y$ complexes can be used as precursors to produce carbon-supported PtRu catalysts with controlled particle size and composition, and that these catalysts are active for methanol electro-oxidation. Catalyst synthesis begins with the formation of G4OH–(Pt^{2+})$_x$(Ru^{3+})$_y$ complexes in aqueous solution. Sequential complexation of Pt^{2+} followed by Ru^{3+} works well because of the strong ligand exchange reaction between the Pt^{2+} precursor and PAMAM's nitrogen atoms. The resulting Pt–N bonds are strong and can withstand pH changes and possible displacement by Ru^{3+} precursor. The UV–vis spectra can be used to follow

the complexation process and show that sequential complexation produces an aqueous, bimetallic complex of Pt^{2+} and Ru^{3+} with G4OH dendrimer.

Catalysts were prepared by impregnation of Vulcan XC-72 carbon black with G4OH–(Pt^{2+})$_x$(Ru^{3+})$_y$ complex solution, followed by drying and activation in H$_2$ gas at elevated temperatures. We systematically investigated the effect of varying activation temperature and Pt:Ru ratio on the physical, chemical, and electrocatalytic properties of the G4OH–Pt$_x$Ru$_y$/C materials. Activation in H$_2$ at elevated temperature results in PAMAM decomposition, reduction of the metal valence, and formation of bimetallic PtRu alloy crystallites. If the activation temperature is too low, incomplete PAMAM decomposition leads to reduced catalytic activity. If the activation temperature is too high, metal particle sintering may occur. In this study, activation at 400 °C was found to be optimal.

We also varied the Ru content from 0 to 50 mol%. In all cases, lattice parameter values from XRD indicate the formation of Pt–Ru alloys, a finding consistent with many previous studies employing other synthesis routes [2,3,6,8,13,14,38,43,44,47,57,64,66–68]. We found that the 50 mol% Ru catalyst gave the best performance for methanol electro-oxidation. We cannot rule out the possibility that somewhat higher Ru content might give better performance, although previous work has found that 50 mol% Ru is optimal.

The main conclusion of this work is that use of PAMAM G4OH in the synthesis recipe leads to small metal particle size, hinders particle sintering during activation at high temperature in H$_2$, and promotes the formation of highly disperse, bimetallic Pt–Ru particles. Omitting G4OH from the recipe gave much larger Pt–Ru alloy particles with very low catalytic activity. The results also suggest that PAMAM G4OH affords fine control over the composition of Pt–Ru catalysts. This method might be extended to explore the efficacy of other promoters besides Ru. Thus PAMAM-mediated synthesis might provide a useful route to highly active catalysts for methanol electro-oxidation with lower precious metal content.

Appendix A. Supplementary data

Supplementary data associated with this article can be found, in the online version, at doi:10.1016/j.jpowsour.2009.07.044.

References

[1] H.S. Liu, C.J. Song, L. Zhang, J.J. Zhang, H.J. Wang, D.P. Wilkinson, J. Power Sources 155 (2006) 95–110.
[2] A.H.C. Sirk, J.M. Hill, S.K.Y. Kung, V.I. Birss, J. Phys. Chem. B 108 (2004) 689–695.
[3] M. Watanabe, S. Motoo, J. Electroanal. Chem. 60 (1975) 267–273.
[4] H.A. Gasteiger, N. Markovic, P.N. Ross, E.J. Cairns, J. Phys. Chem. 97 (1993) 12020–12029.
[5] P.K. Shen, A.C.C. Tseung, J. Electrochem. Soc. 141 (1994) 3082–3090.
[6] D. Kardash, C. Korzeniewski, N. Markovic, J. Electroanal. Chem. 500 (2001) 518–523.
[7] C. Lu, C. Rice, R.I. Masel, P.K. Babu, P. Waszczuk, H.S. Kim, E. Oldfield, A. Wieckowski, J. Phys. Chem. B 106 (2002) 9581–9589.
[8] B.J. Hwang, C.H. Chen, L.S. Sarma, J.M. Chen, G.R. Wang, M.T. Tang, D.G. Liu, J.F. Lee, J. Phys. Chem. B 110 (2006) 6475–6482.
[9] B.J. Hwang, L.S. Sarma, J.M. Chen, C.H. Chen, S.C. Shih, G.R. Wang, D.G. Liu, J.F. Lee, M.T. Tang, J. Am. Chem. Soc. 127 (2005) 11140–11145.
[10] D.G. Liu, J.F. Lee, M.T. Tang, J. Mol. Catal. A: Chem. 240 (2005) 197–206.
[11] P.K. Babu, J.H. Chung, S.T. Kuk, T. Kobayashi, E. Oldfield, A. Wieckowski, J. Phys. Chem. B 109 (2005) 2474–2477.
[12] Y.Y. Tong, H.S. Kim, P.K. Babu, P. Waszczuk, A. Wieckowski, E. Oldfield, J. Am. Chem. Soc. 124 (2002) 468–473.

[13] M.S. Nashner, A.I. Frenkel, D.L. Adler, J.R. Shapley, R.G. Nuzzo, J. Am. Chem. Soc. 119 (1997) 7760–7771.
[14] M.S. Nashner, A.I. Frenkel, D. Somerville, C.W. Hills, J.R. Shapley, R.G. Nuzzo, J. Am. Chem. Soc. 120 (1998) 8093–8101.
[15] L. Dubau, F. Hahn, C. Coutanceau, J.-M. Leger, C. Lam, J. Electroanal. Chem. 554–555 (2003) 407–415.
[16] J. Guo, G. Sun, S. Shiguo, Y. Weiqian, Q.J. Yushan, X. Qi, J. Power Sources 168 (2007) 299–306.
[17] M. Ueji, M. Harada, Y. Kimura, J. Colloid Interface Sci. 322 (2008) 358.
[18] T. Vidakovic, M. Christov, K. Sundmacher, K. Nagabhushana, W. Fei, H.B.S. Kinged, Electrochim. Acta 52 (2007) 2277.
[19] H. Tu, W. Wang, C. Wan, Y. Wang, J. Phys. Chem. B 110 (2006) 15988.
[20] H. Li, G. Sun, Y. Gao, Q. Jiang, Z. Jia, Q. Xin, J. Phys. Chem. C 111 (2007).
[21] H. Nitani, T. Nakagawa, H. Daimon, Y. Kurobe, T. Ono, Y. Honda, A. Koizumi, S. Seino, T.A. Yamamoto, Appl. Catal. A 326 (2007) 194.
[22] L. Li, Y. Xing, J. Phys. Chem. C 111 (2007) 2803.
[23] D. Geng, L. Chen, G. Lu, J. Mol. Catal. A: Chem. 265 (2007) 42.
[24] L. Sarma, C. Chen, S. Kumar, G. Wang, S. Yen, D.-G. Liu, H.-S. Sheu, K.-L. Yu, M.-T. Tang, J.-F. Lee, C. Bock, K.-H. Chen, B.-J. Hwang, Langmuir 23 (2007) 5802.
[25] O. Petrii, J. Solid State Electrochem. 12 (2008) 609.
[26] R.M. Crooks, B.I. Lemon, L. Sun, L.K. Yeung, M.Q. Zhao, Top. Curr. Chem. 212 (2001) 81–135.
[27] R.M. Crooks, M.Q. Zhao, L. Sun, V. Chechik, L.K. Yeung, Acc. Chem. Res. 34 (2001) 181–190.
[28] Y.H. Niu, R.M. Crooks, C. R. Chim. 6 (2003) 1049–1059.
[29] R.W.J. Scott, A.K. Datye, R.M. Crooks, J. Am. Chem. Soc. 125 (2003) 3708–3709.
[30] M.Q. Zhao, R.M. Crooks, Angew. Chem. Int. Ed. 38 (1999) 364–366.
[31] M.Q. Zhao, R.M. Crooks, Adv. Mater. 11 (1999) 217–220.
[32] M.Q. Zhao, R.M. Crooks, Chem. Mater. 11 (1999) 3379–3385.
[33] G. Lafaye, A. Siani, P. Marecot, M.D. Amiridis, C.T. Williams, J. Phys. Chem. B 110 (2006) 7725–7731.
[34] G. Lafaye, C.T. Williams, M.D. Amiridis, Catal. Lett. 96 (2004) 43–47.
[35] H. Xie, Y.L. Gu, H.J. Ploehn, Nanotechnology 16 (2005) S492–S501.
[36] A.J. Dickinson, L.P.L. Carrette, J.A. Collins, K.A. Friedrich, U. Stimming, Electrochim. Acta 47 (2002) 3733–3739.
[37] K.A. Friedrich, K.P. Geyzers, A.J. Dickinson, U. Stimming, J. Electroanal. Chem. 524 (2002) 261–272.
[38] Y. Takasu, T. Fujiwara, Y. Murakami, K. Sasaki, M. Oguri, T. Asaki, W. Sugimoto, J. Electrochem. Soc. 147 (2000) 4421–4427.
[39] G. Larsen, E. Lotero, M. Marquez, Chem. Mater. 12 (2000) 1513.
[40] G. Larsen, S. Noriega, Appl. Catal. A 278 (2004) 73–81.
[41] H.C. Ye, R.W.J. Scott, R.M. Crooks, Langmuir 20 (2004) 2915–2920.
[42] H.P. Klug, L.E. Alexander, X-ray Diffraction Procedures for Polycrystalline and Amorphous Materials, Wiley, New York, 1974, xxv, 966 pp.
[43] V. Radmilovic, H.A. Gasteiger, P.N. Ross, J. Catal. 154 (1995) 98–106.
[44] B. Beden, F. Kadirgan, C. Lamy, J.M. Leger, J. Electroanal. Chem. 127 (1981) 75–85.
[45] S. Hadzijordanov, H. Angersteinkozlowska, M. Vukovic, B.E. Conway, J. Electrochem. Soc. 125 (1978) 1471–1480.
[46] E.A. Seddon, K.R. Seddon, The Chemistry of Ruthenium, Elsevier, Amsterdam, 1984.
[47] Z.L. Liu, X.Y. Ling, X.D. Su, J.Y. Lee, J. Phys. Chem. B 108 (2004) 8234–8240.
[48] J. Charlier, V. Detalle, F. Valin, C. Bureau, G. Lecayon, J. Vac. Sci. Technol. A 15 (1997) 353–364.
[49] A.J. Wagner, G.M. Wolfe, D.H. Fairbrother, Appl. Surf. Sci. 219 (2003) 317–328.
[50] O. Ozturk, T.J. Black, K. Perrine, K. Pizzolato, C.T. Williams, F.W. Parsons, J.S. Ratliff, J. Gao, C.J. Murphy, H. Xie, H.J. Ploehn, D.A. Chen, Langmuir 21 (2005) 3998–4006.
[51] E. Laksono, A. Galtayries, C. Argile, P. Marcus, Surf. Sci. 530 (2003) 37–54.
[52] J.C. Vickerman (Ed.), Surface Analysis: The Principal Techniques, John Wiley and Sons, New York, 1997.
[53] J.P. Contour, G. Mouvier, M. Hoogewys, C. Leclere, J. Catal. 48 (1977) 217–228.
[54] V.I. Nefedov, Y.V. Salyn, I.B. Baranovskii, A.G. Maiorova, Zh. Neorg. Khim. 25 (1980) 216–225.
[55] Y.V. Salyn, V.I. Nefedov, A.G. Maiorova, G.N. Kuznetsova, Zh. Neorg. Khim. 23 (1978) 829–831.
[56] C.D.R. Wagner, W.M. Rigs, L.E. Davis, J.F. Moulder, Handbook of X-ray Photoelectron Spectroscope, Perkin Elmer Corporation, Eden Prairie, MN, 1978.
[57] A.S. Arico, P. Creti, H. Kim, R. Mantegna, N. Giordano, V. Antonucci, J. Electrochem. Soc. 143 (1996) 3950–3959.
[58] B. Folkesso, Acta Chem. Scand. 27 (1973) 287–302.
[59] J.C. Fuggle, T.E. Madey, M. Steinkilberg, D. Menzel, Surf. Sci. 52 (1975) 521–541.
[60] R. Nyholm, N. Martensson, J. Phys. C: Solid State Phys. 13 (1980) L279–L284.
[61] C.S. Huang, M. Houalla, D.M. Hercules, C.L. Kibby, L. Petrakis, J. Phys. Chem. 93 (1989) 4540–4544.
[62] K.S. Kim, N. Winograd, J. Catal. 35 (1974) 66–72.
[63] D.D. Sarma, C.N.R. Rao, J. Electron. Spectrosc. Relat. Phenom. 20 (1980) 25–45.
[64] J. Solla-Gullon, F.J. Vidal-Iglesias, V. Montiel, A. Aldaz, Electrochim. Acta 49 (2004) 5079–5088.
[65] C.T. Williams, personal communication.
[66] E. Antolini, L. Giorgi, F. Cardellini, E. Passalacqua, J. Solid State Electrochem. 5 (2001) 131–140.
[67] D. Chu, S. Gilman, J. Electrochem. Soc. 143 (1996) 1685–1690.
[68] C.A. Angelucci, M. D'Villa Silva, F.C. Nart, Electrochim. Acta 52 (2007) 7293–7299.